Full title:

Material point method simulation of pile penetration in sand considering the effects of grain breakage

S. Fu[1], Z.X. Yang[2], N. Guo[3], R.J. Jardine[4]

[1] Graduate student, Department of Civil Engineering, Zhejiang University, Hangzhou, 310058, China. Email: 11912013@zju.edu.cn;
[2] Professor, Department of Civil Engineering, Zhejiang University, Hangzhou, 310058, China, Email: zxyang@zju.edu.cn; corresponding author;
[3] Assistant Professor, Department of Civil Engineering, Zhejiang University, Hangzhou, 310058, China. Email: nguo@zju.edu.cn;
[4] Professor, Department of Civil and Environmental Engineering, Imperial College London, SW7 2AZ, UK. Email: r.jardine@imperial.ac.uk;

Contact person:

Z. X. Yang, PhD
Professor in Geomechanics
Department of Civil Engineering
Zhejiang University
B712, Anzhong Building
Zijingang campus
Hangzhou 310058, China
Tel: 86 (0)571 8820 8476
Email: zxyang@zju.edu.cn

Material point method simulation of pile penetration in sand considering the effects of grain breakage

Abstract: All full displacement installation processes dramatically alter the stress and strain fields applying around piles inserted in sand. Calibration chamber tests have indicated that severe particle crushing occurs near to the pile tip and a distinct shear zone may develop that leaves crushed sand adhering to the pile shaft. It appears to be important to investigate how particle breakage affects the stress and deformation fields developed as this process occurs. In this study, the installation by monotonic jacking of a conically tipped model pile into silica sand is simulated by material point method (MPM) analyses. A thermodynamically consistent model which considers competing grain crushing and dilation is employed to model the sand behavior, while an MPM approach is adopted to cater for the large deformations involved in the penetration process. Particle crushing is predicted beneath the pile tip and around the pile shaft. The numerical results are compared to directly related instrumented pile calibration chamber tests. Remarkably, the numerical results show that the computed stress and displacement fields match the experimental results well, especially in reproducing the volumetric compression observed experimentally. The results confirm that combining MPM with suitably sophisticated constitutive models creates new capabilities for analyzing large-deformation problems.

Keywords:

driven piles; sand; calibration chamber; material point method; grain crushing; volumetric strain

1. Introduction

This paper is concerned with the related problems of displacement pile installation and cone

penetration testing (CPT) in sand. Both topics are of interest to geotechnical engineering worldwide and CPT profiling has been central to improving methods for designing driven piles to take axial loading. Modern 'CPT-based' design methods (see for example Jardine et al. 2005, Yang et al. 2017, Lehane et al. 2017, Lehane et al. 2020) have far better accuracy and reliability than the traditional 'earth-pressure' methods such as the 'main-text' API (American Petroleum Institute, see API RP2GEO 2014) approach and appear set to become the main International Organization for Standardization (ISO) method for offshore pile design. Nevertheless, the theoretical link between CPT penetration resistance and several aspects of driven pile behavior remain open to exploration and improvement, including the well-known tendency for piles driven in sand to develop marked increases in axial capacity over the months that follow driving (see Jardine et al. 2006, Cathie et al. 2022). This paper contributes to future improvement of design methods' predictive accuracy and reliability by studying of the physics that links the CPT and pile penetration processes.

Field and laboratory experimental investigations of the stress conditions induced by pile penetration include several studies with heavily instrumented piles (see Lehane et al. 1993, Chow 1997, Jardine et al. 2005, Yang et al. 2010, Tsuha et al. 2012, Jardine et al. 2013a, b). The deformation and strain fields developed in sand masses surrounding a penetrometer have also been investigated in the laboratory through early X-ray film photogrammetry (Robinsky et al. 1964, Chong et al. 1988, Otani et al. 2005, Ngan-Tillard et al. 2005) and optical techniques, such as particle image velocimetry (PIV) (White 2002; White and Bolton 2004; Liu 2010; Mo et al. 2015) and digital image correlation (DIC) (Arshad 2014; Arshad et al. 2014; Tovar-Valencia et al. 2018; Ganju et al. 2020; Tovar-Valencia et al. 2023). It is well-known that during the pile installation into sand, even silica sand, involves varying degrees of breakage, owing to the extremely high stress

level in the pile tip and large displacement interface shearing processes (Yasufuku and Hyde 1995; Gavin and Lehane 2003; White and Bolton 2004; Yang et al. 2010; Arshad et al. 2014; Tovar-Valencia et al. 2023) which can also be studied in suitably large displacement ring-shear interface tests combined with optical grain measuring techniques (see Ho et al. 2011). Particles crushed beneath the pile tip are displaced radially as penetration advances and a significant proportion are gradually aggregated into a sorted thin layer adhering to the pile shaft. This thin layer of highly crushed particles also acts as a shear band that significantly affects the pile–soil interaction response and shaft capacity of displacement piles. Other studies that investigated the effects of particle breakage on pile bearing capacity, displacement field and soil densification during pile driving include Yasufuku and Hyde (1995), who discussed the relationship between driven pile bearing capacity and load–displacement behavior in crushable sands. Klotz and Coop (2001) also considered how shaft interface friction characteristics are affected by particle breakage, which they related to the sands' states and pile base resistances. Plane-strain calibration chamber tests conducted by White and Bolton (2004) suggested that particle breakage near the pile shaft might lead to outward migration of fines into the surrounding void spaces in the sand matrix, leading to further radial contraction and normal stress reduction acting on the shaft. Through half-pile calibration chamber tests and DIC measurements, Tehrani et al. (2018) observed a volume contraction in loose sand and dilation in dense sand within 1*R* (*R* = pile radius) region from the shaft; any tendency of the fine crushed particles to migrate and fill the voids between coarser particles could potentially reduce the impact of any dilation that develops at the pile shaft-sand interface. Ganju et al. (2020) computed the volumetric strain increments developed around penetrometers in medium-dense and dense sands and reported contraction adjacent to the penetrometer surfaces in both medium-

dense and dense sand, while the sands' responses were found to be dilative further away from the penetrometer. The sand volume changes reflect the contributions from both (plastic) particle rearrangement and particle breakage.

While field and laboratory experiments have provided vital information regarding displacement pile installation, numerical simulations offer the potential to obtain in an efficient manner more detailed information regarding the stress and strain fields (Ciantia et al. 2019, Wang and Zhao 2014, Yang et al. 2020, Gao et al. 2022, Fu et al. 2023, Guo et al. 2023). Existing high-quality experimental datasets provide benchmarks against which the relevance and accuracy of potential numerical simulations can be assessed (Yang et al. 2020; Fu et al. 2023). Yang et al. (2020) presented arbitrary Lagrangian-Eulerian (ALE) analyses of the highly instrumented 'Grenoble' calibration chamber tests of displacement piles reported by Jardine et al. (2013a, b). They used a simple Mohr–Coulomb model with state dependent parameters that did not consider particle breakage in the same way as Zhang et al. (2014). Fu et al. (2023) obtained the displacement and strain fields applying during monotonic pile jacking using the same method by Yang et al. (2020) and speculated considering particle breakage would offer a way of developing still more accurate numerical simulations of the experiments. However, ALE analyses suffer from inherent difficulties related to mesh distortion, numerical convergence and mesh sensitivity. In addition, ALE analyses incorporating more advanced constitutive models may struggle to re-mapping the state parameters accurately and can predict stress states that lie outside the yield surface for plasticity models (Salgado et al. 2022). In contrast, the material point method (MPM) does not require state variable remapping because the variables are carried by the material points throughout the computation.

MPM has gradually matured as a numerical tool for geotechnical analyses involving large-deformation and has gained more widespread use (see Andersen and Andersen. 2010, Soga et al., 2016, de Vaucorbeil et al. 2020). Gao et al. (2022) recently simulated jacked pile penetration successfully using MPM with an improved pile–soil contact model obtaining reasonable matches with calibration chamber test results. This paper investigates whether incorporating grain breakage leads to still further improved predictions.

Zhang et al. (2013, 2014) presented a pioneering ALE simulation of pile penetration into sand employing a simple linear elastic breakage model proposed by Einav (2007a, b). The particle breakage contours were successfully reproduced beneath the pile tip and along the shaft and matched well the experimental results of Yang et al. (2010), along with the tip resistance q_c profiles and the stresses developed within the sand mass during the penetration. However, the sand's dilation was not considered fully in the energy dissipation and the linear elasticity adopted in calculating the free energy in their simplified breakage model did not allow the density variations within the sand to be tracked during the pile penetration. Jin et al. (2018) introduced particle breakage into a multi-surface plasticity model to address its influence on bearing capacity in sand using the finite element method. However, the volumetric strain of sand due to the particle breakage was not considered in their study, which could be important in realistically simulating the stresses and deformations induced by displacement pile installation.

No pile penetration study employing both MPM and particle breakage appears to have been reported to date (see Lorenzo et al. 2017, Martinelli et al. 2021, Salgado et al. 2022, Gao et al. 2022, Yost et al. 2023). The Authors' MPM study of pile penetration into sand employed a thermodynamics-based, micromechanically inspired, constitutive sand breakage approach

proposed by Tengattini et al. (2016) that addresses the effect of the evolving cumulative grain size distribution (GSD). The study is presented as follows.

- Section 2 recapitulates the principles of MPM and introduces the sand breakage and dilatancy model. Some numerical aspects for the MPM simulation of CPT are also set-out, including the techniques adopted to ensure stability and accuracy. The proposed model's predictive capabilities are assessed by considering element tests on two of the sands (Fontainebleau NE34 and #2Q-ROK) employed in high-quality 'Grenoble' and 'Purdue' calibration chamber model pile experiments.
- Section 3, the stress fields developed during and after pile penetration are simulated and compared to the 'Grenoble' calibration chamber tests. The strain and deformation fields measured in the 'Purdue' tests are also presented and compared to the numerical simulation, with the role of particle breakage being highlighted.
- Section 4 presents the study's main conclusions.

2. Numerical model

2.1 A brief description of the MPM formulation

MPM is a numerical method particularly suited to modelling history-dependent behaviour in large-deformation geotechnical problems (Phuong et al. 2016; Soga et al. 2016; Lorenzo et al. 2018; Martinelli et al. 2021; Gao et al.2022; Salgado et al. 2022). The MPM calculation domain comprises Lagrangian particles within an Eulerian grid. Each particle has an associated position, mass, density, velocity, deformation gradient and any other internal state variables required for the constitutive material models. The balance of momentum equation is solved in the background grid. Material

point discretization is generated derivatively by the structure of the grid, and the initial number of material points per element is specified across the grid. The material points which carry all the physical information can move freely through the elements, so the mesh distortion problem can be largely avoided. However, the movement of particles in MPM can generate numerical instabilities, such as cell crossing errors triggered by the discontinuity of the derivative of the interpolation function. This phenomenon can be alleviated by several methods (Bardenhagen and Kober, 2004, Sadeghirad et al., 2011, Steffen et al., 2008, Zhang et al., 2011). An effective and widely accepted generalized interpolation material point (GIMP) formulation, i.e., uGIMP (undeformed GIMP), which assumes that the particle domain unchanged during the simulations, is adopted in this study. It is known that the material point integration scheme in MPM can lead to some loss of accuracy compared to the Gaussian integration in FEM. The error arises from the integration scheme is approximate and sums data from a set of material points, which may not be uniformly distributed or capture all the features of the solution accurately (Salgado et al. 2022). In this study, the stability and accuracy of the results are enhanced by an advanced soil–pile interface contact detection algorithm, momentum modification, iterative stress integration and finer grids. These modifications in the numerical algorithms and the adoption of credible constitutive models of MPM improve the accuracy of CPT penetration analyses (Yost et al. 2023).

2.2 Constitutive model

The breakage theory proposed by Einav (2007a, b) rigorously considers the effects of the evolving cumulative grain size distribution (GSD) due to sand particle crushing on the material behaviour, by introducing an internal breakage variable *B* within the thermodynamics framework. Compared to the “student breakage model” adopted in the simulations of Zhang et al. (2013, 2014),

pressure-dependent elasticity is incorporated into the formulation and the porosity of sand is also introduced directly as an internal variable in the breakage model (Tengattini et al. 2016). The pressure dependent Helmholtz free energy potential can be expressed as,

$$\Psi = (1- \theta B)\left(p_r \frac{2}{3}\frac{A^2}{\bar{K}} + p_r \frac{3}{2}\bar{G}A\left(\varepsilon_s^e\right)^2 \right) \tag{1}$$

where θ is the grading index which measures the distance between the initial and ultimate GSDs; B is an internal variable which predicts the current cumulative GSD through a linear scaling between the initial and ultimate cumulative GSDs; p_r is a reference pressure (conveniently taken as 1 kPa); $A = \frac{\bar{K}}{2}\varepsilon_v^e + 1$; ε_v^e and ε_s^e are the volumetric and shear elastic strains, respectively; $\bar{K}$ and $\bar{G}$ are non-dimensional bulk and shear stiffness coefficients, respectively.

In the thermodynamic framework, the form of stress variables can be deduced from the Helmholtz free energy. E_B is the stress-like conjugate to B, termed breakage energy, as given below,

$$E_B = -\frac{\partial \Psi}{\partial B} = \theta p_r \left(\frac{2}{3}\frac{A^3}{\bar{K}} + \frac{3}{2}\bar{G}A\left(\varepsilon_s^e\right)^2 \right) \tag{2}$$

$$p = \frac{\partial \Psi}{\partial \varepsilon_v^e} = (1-\theta B)\left(p_r A^2 + \frac{3}{4}\bar{K}\bar{G}\left(\varepsilon_s^e\right)^2 \right) \tag{3}$$

$$q = \frac{\partial \Psi}{\partial \varepsilon_s^e} = 3(1-\theta B)\, p_r \bar{G}\varepsilon_s^e \tag{4}$$

The yield function is derived from the explicit form of dissipation rate function (Tengattini et al. 2016):

$$y = \left[\sqrt{\frac{E_B}{E_C}}(1-B) - \gamma\tau \right]^2 + \left(\frac{q}{Mp} \right)^2 - 1 \tag{5}$$

where E_C is the critical breakage energy (with the dimension of stress); γ is a material parameter controlling the dilation potential; M is the critical state stress ratio at triaxial compression. The 'relative porosity' τ is defined as followings, with ϕ_{max}, ϕ_{min} and ϕ the maximum, minimum and

current porosities, respectively:

$$\tau = \frac{\phi_{\max} - \phi}{\phi_{\max} - \phi_{\min}} \tag{6}$$

The flow rules are defined in a way that does not violate the second law of thermodynamics (Tengattini et al. 2016):

$$\dot{B} = \lambda \frac{\partial y^*}{\partial E_B} = 2\lambda \left\langle \sqrt{\frac{E_B}{E_C}}(1-B) - \gamma\tau \right\rangle \frac{1-B}{\sqrt{E_B E_C}} \cos^2 \omega \tag{7}$$

$$\dot{\phi} = \lambda \frac{\partial y^*}{\partial E_\phi} = 2\lambda \left[\sqrt{\frac{E_B}{E_C}}(1-B) - \gamma\tau \right] \frac{E_B}{E_\phi} \sin^2 \omega \tag{8}$$

$$\dot{\varepsilon}_p^s = \lambda \frac{\partial y^*}{\partial q} = 2\lambda \frac{q}{(Mp)^2} \tag{9}$$

where λ is a non-negative multiplier. The flow rules are the direct results of the definition of an explicit non-negative dissipation rate equation. Note that the presence of the Macaulay brackets function <> in Eq. (7) ensures that crushing is connected strictly to grain size reduction.

Table 1 Constitutive parameters of the breakage model (Fontainebleau sand).

Mechanical parameters					Index properties				
$\bar{K}$	$\bar{G}$	E_c(MPa)	M	γ	α_u	α_l	u'	l	θ
600	452	1.42	1.35	0.9	0.474	0.338	0.3	0.3	0.6

Fontainebleau sand is a standard fine siliceous uniform test sand (Dano et al., 2004). Yang et al. (2010) gave full details of the sand's mineralogy, grain shapes and size distribution curve. The mechanical properties have been reported by Luong and Touati, (1983), Andria-Ntoanina et al. (2010), and Altuhafi et al. (2018). The breakage properties of Fontainebleau sand in the simulations have been determined from these data by the available element tests, as summarized in Table 1. The index properties α_l and α_u are the lower and upper limit porosities at zero breakage, and the coefficients *l* and *u*' depend on the grain shape and roughness. The determination of index

properties are referred to Tengattini et al. (2016). According to Nguyen and Einav (2009), $\bar{K}$ and $\bar{G}$ should satisfy the following equation for the stability: $\frac{\bar{G}}{\bar{K}} > \frac{M^2}{3}$. The non-dimensional bulk and shear stiffness coefficients, $\bar{K}$ and $\bar{G}$ of Fontainebleau sand were deduced from the Poisson's ratio and the Young modulus based on a series of triaxial experiments by Dano et al. (2004) at the confining pressure of 100 kPa. The critical breakage energy E_C can be expressed in terms of the yield pressure p_{cr} in the isotropic compression, as given by Zhang et al. (2013). Furthermore, following Altuhafi et al. (2018), the friction coefficient is taken as M = 1.35, calculated from the effective friction angle of 33°. γ is taken as the value recommended by Tengattini et al. (2016). Other index properties in the table are taken from Yang et al. (2010). Model responses of triaxial tests on a wide range of confining pressures (Luong and Touati, 1983; Andria-Ntoanina et al. 2010) are compared with the experimental results, as shown in Fig. 1. It can be seen that under low confining pressures (= 400 kPa), the strain-hardening and dilative behaviour can be well captured by the model. In contrast, under high confining pressures (up to 16 MPa), the deviatoric stress simulated by the model is comparable to the experimental result, while the dilative volumetric strains are highly over-predicted.

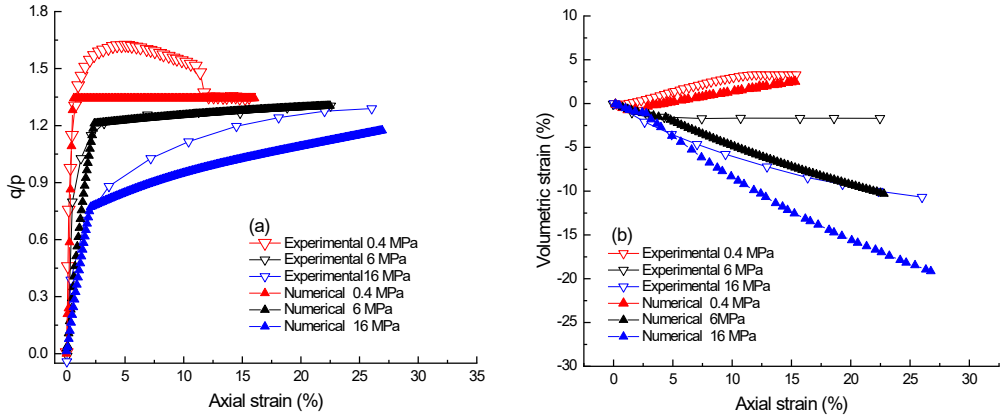

Fig. 1. Simulation results of triaxial tests on Fontainebleau NE34 sand: (a) q/p–ε_a from low to high confining pressures; (b) ε_v–ε_a from low to high confining pressures (up to 16 MPa)

2.3 Contact formulation

The MPM deals with the contact between different materials referenced to the background grid nodes. Bardenhagen et al. (2001) introduced the multi-velocity field to deal with the contact and separation between different objects. This method assumes that there is no penetration between different objects. However, the stiffnesses of soils and structural materials are usually so different that the initial contacts involved in soil–structure interaction problems are prone to produce unrealistic "impact" effects which disturb to the nodes' accelerations and velocities and lead to severe numerical disturbance and contact force errors that have a dramatically adverse effect on the node momentum in an interface modelling. In addition, in the process of contact detection, Bardenhagen's contact algorithm (Bardenhagen et al. 2000, Bardenhagen et al. 2001) maps the mass and velocity information of material points to the grid, and then corrects the contact forces. Consequently, when gaps open between the structure surface and soil, erroneous force corrections may be made on those areas of the structure and soil that were previously in contact.

Therefore, it is imperative to improve the traditional detection of material point contact algorithm. Penalty functions are usually introduced to adjust the contact force application process between the soil and structure interface, thus enhancing the stability of the contact algorithm (Ma et al. 2014, Dong 2020, Gao et al. 2022). In this study, a modified algorithm based on Bardenhagen et al. (2000)'s contact approach but incorporating Hammerquist et al. (2018)'s analytical expression is applied and implemented in the MPM simulations in the open source code NairnMPM (Gao et al. 2022). The modified contact algorithm can eliminate the gap between the structure and soil and also yield a smoother contact force calculation curve, which facilitates the improvement of

numerical stability in the calculation process dealing with the pile–soil contact. The smoothing parameters are set to α = 1 and β = 20, as recommended in Gao et al. (2022).

2.4 Stress integration algorithm

A semi-implicit integration technique introduced by Zhang (2012) is employed to avoid the convergence difficulties caused by large strain increments in the plastic corrector of the proposed model. However, due to the linearization (i.e., first-order Taylor expansion) of the yield function, the returned stress point usually does not exactly lie on the subsequent yield surface. The repetition of the above process, e.g., linearizing the yield function at trial stress point and then following the same algorithm is a simple way to reduce the discrepancy between the stress point and the yield surface.

2.5 Mesh sensitivity

Mesh convergence analysis is crucial in verifying the accuracy of MPM simulations. Convergence analyses are conducted to identify the optimal mesh density and reduce the computational cost while achieving the required solution accuracy. Three mesh sizes, with 4 particles in each element, were applied in the pile penetration simulations to conduct the mesh convergence analysis. The grid sizes used in this study were 0.018 m, 0.009 m, and 0.0045 m, which led to computational costs of 14, 42 and 122 hours respectively to complete each simulation employing an 8-core AMD Ryzen 7 CPU. The solutions' sensitivity to mesh geometry was checked by comparing the cone resistance q_c profiles. The predicted pile tip resistances tend most convincingly to the experimentally measured 20 MPa asymptote (Jardine et al. 2013a, b) with the finest mesh (=0.0045 m) which was therefore adopted for the main study.

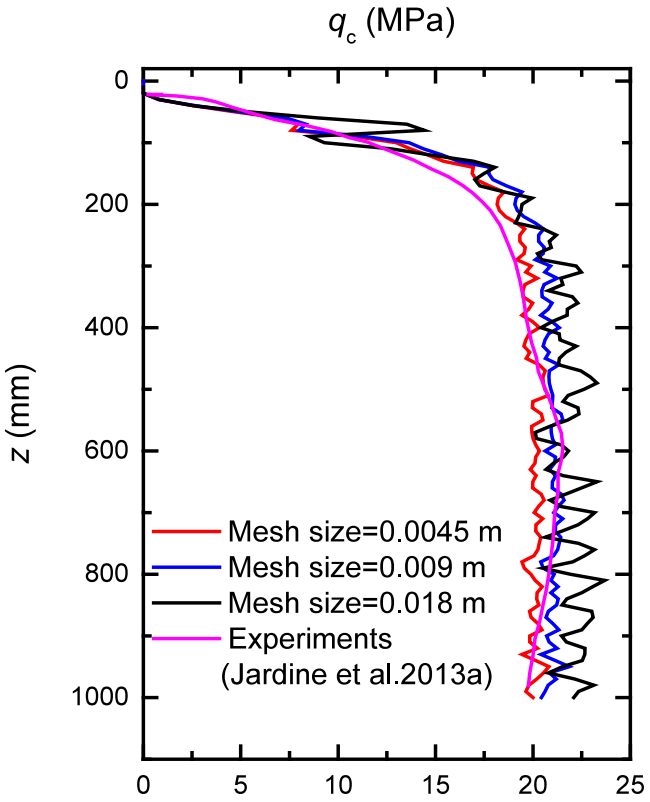

Fig. 2 Sensitivity analyses in different mesh sizes.

3. MPM analysis of calibration chamber experiments

The MPM analysis with breakage model was verified against two series of experiments: the highly instrumented Grenoble calibration chamber tests (Jardine et al. 2013a, b) and the 'half' pile calibration chamber penetration experiments using digital image correlation (DIC) conducted at Purdue University (Arshad 2014, Arshad et al. 2014).

3.1 Simulation of Grenoble calibration chamber test- verification of stress field

The Grenoble calibration chamber test results (Jardine et al. 2013b) are used first to verify the stress fields. The pile is considered as rigid and the interface between the pile and sand is modelled by the modified Bardenhagen's contact algorithm (Gao et al. 2022). The breakage model developed by Tengattini et al. (2016) is used to describe the crushable Fontainebleau sand behaviour in the numerical simulations and the model parameters are calibrated by comparing the model responses

with the triaxial test results. The axially symmetric MPM model is illustrated in Fig. 3, along with boundary conditions and model dimensions, are taken to be the same as in the experiments. In the simulation, the vertical pressure was gradually elevated to 150 kPa over the upper surface of the sand mass, before advancing the pile at a constant velocity into the 'chamber'. The model parameters of the Fontainebleau sand used in the simulation were introduced in Section 2.2. Other parameters are from Yang et al. (2010), including the soil–pile interface friction coefficient = 0.49 calculated from the measured interface friction angle 26°, and the dry unit weight of sand = 16.3 kN/m^3.

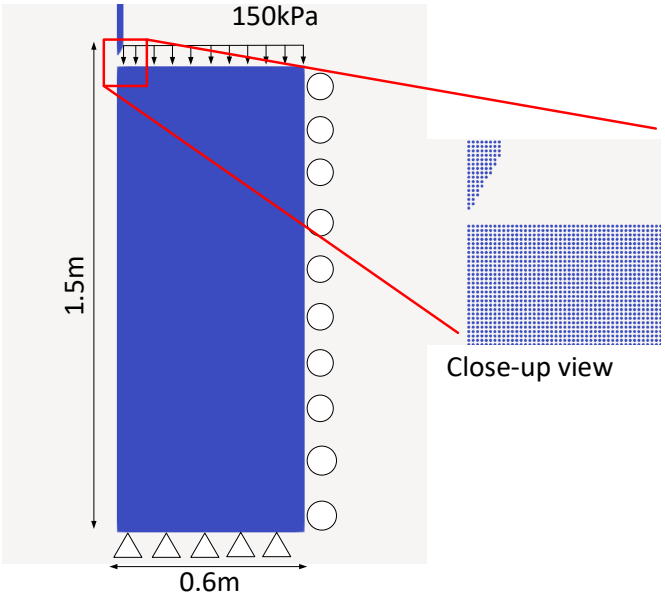

Fig. 3. Geometry and boundary conditions of the numerical model

A comparison of the tip resistance q_c profiles between the calibration chamber test and the simulation results, plotted against the normalized penetration depth (L_p) is presented in Fig. 4. The numerical results show a general agreement with the experiments, and q_c increases rapidly in the shallow depth (<10R) region before gradually approaching a quasi-steady value which persists to the final penetration depth. The numerical profile of q_c is used in the following data interpretation and analysis, following the same approach described in Jardine et al. (2013a, b).

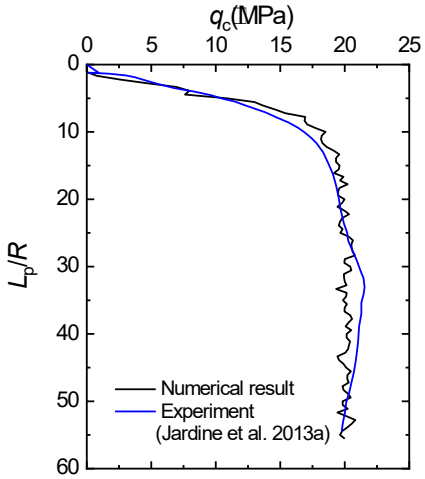

Fig. 4. Comparison of cone tip resistance profiles

Fig. 5 shows the evolution of radial stresses normalized with q_c, at r/R = 2 with three different penetration depths L_p. Excellent matches with the experimental "moving" stress results are observed, showing the radial stresses increasing sharply as the tip approaches the stress sensors' level (or penetration depth) and falling steeply immediately after the tip passes by.

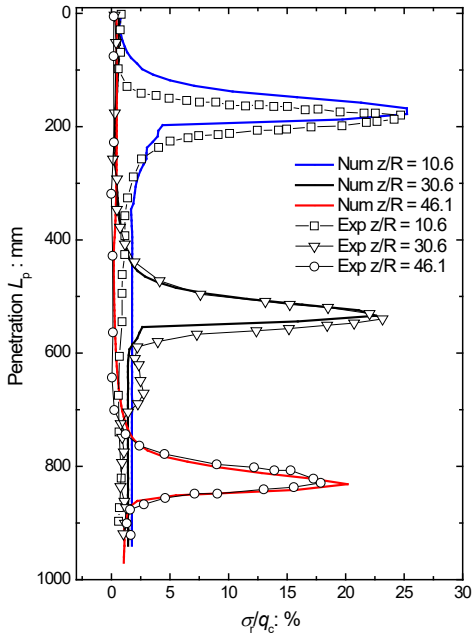

Fig. 5. Normalised radial stresses measured at r/R = 2 during penetration

As reported by Yang et al. (2010) and Arshad et al. (2014), a thin layer composed of highly crushed particles formed and adhered to both model piles' shafts after undergoing the extremely

high stress and large deformation penetration process. The observed particle crushing can be simulated by the breakage model in the study. Fig. 6(a) presents the breakage contour of crushing index B for the penetration depth of 20R. For clarity, only B values greater than 0.01 are shown. The most prominent zone of crushing zone falls within an annulus of approximately 1R width around the pile shaft. Below the cone tip, the breakage index B decays from 0.3 to 0.01, extending vertically to $h/R \approx -2$ and radially to $r/R \approx 2$. Arshad et al. (2014)'s DIC results indicate that sand undergoing severe-to-moderate breakage extends out to 1.3R from the axis of the closed-ended pile's shaft, consistent with the $B > 0.1$ range shown in Fig. 6(a). Intuitively, the assembly of particles adjacent to the pile shaft would contract as breakage continues under continuous shearing, as occurs in ring-shear interface tests (Ho et al. 2011). However, the contour lines of index B are approximately parallel to the pile axis, suggesting that further particle crushing along the shaft is relatively minor as installation proceeds. It is recognized though that the MPM model does not fully capture potential micro-mechanical interactions between the grains and the topography of the rough pile shaft. As the cone tip continues to penetrate, the highly crushed displaced particles endure intense shear and compression and form a dense shear band around the advancing shaft that significantly affects the volumetric strains around the pile shaft. Figs. 6(b)–(d) display the comparison between the predicted and the experimental cumulative grain size distributions (GSDs) in three different zones, respectively (Yang et al. 2010). The initial and ultimate GSDs are illustrated in these plots. The severe particle crushing applying at point A in Fig. 6(b), leads to a significant alteration of the virgin GSD. While the numerically simulated GSD shown in Fig. 6(b) (particle size finer than 0.07 mm) appears inconsistent with the experimentally observed 'crushed' sand GSD over its finer size range, this disparity is thought to reflect the limited resolution of the QicPic

imaging device employed in Yang et al. (2010) to investigate small samples taken from around the pile shaft.

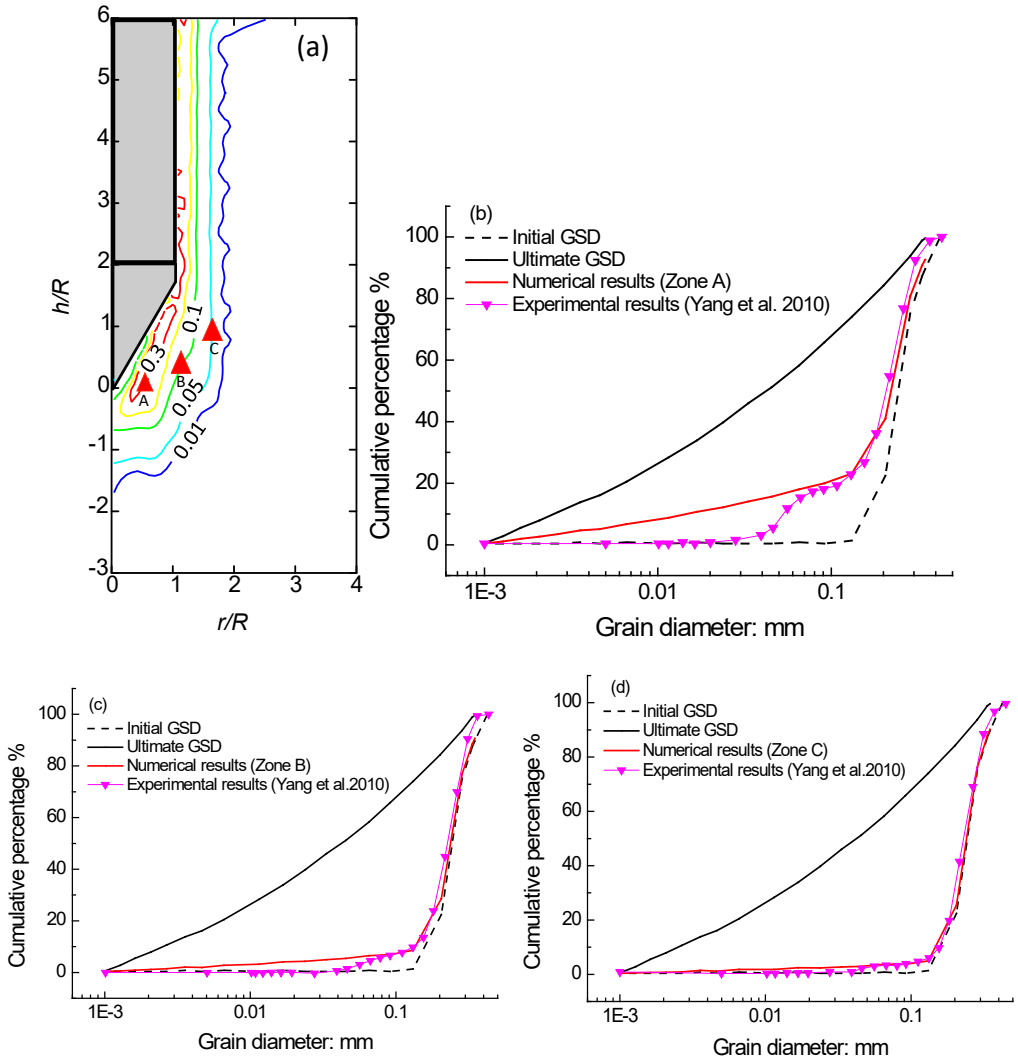

Fig. 6. Simulated crushing profile and grain size distribution (a) profile of crushing zones, (b) zone A, (c) zone B, (d) zone C

Fig. 7 presents the radial and circumferential stresses developed at three levels covering 6 < h/R < 30 above the pile tip after the penetration. The predicted stress variations with radial distance r/R match well the experimental measurements in the calibration chamber tests (Jardine et al. 2013b), reflecting the dependence of local shaft friction resistance on the tip relative position h/R. The distribution profiles indicate that the normal stress maxima within the sand mass do not develop on the shaft surface (r/R = 1) but at more radially distant positions, as seen in experiments

(Jardine et al. 2013b) and other numerical results (Yang et al. 2020, Gao et al. 2022, Fu et al. 2023). The local stress relaxation near the pile shaft is well captured with the breakage model. In contrast to the simulations made without considering particle breakage (Yang et al. 2020), where no contractive volumetric strain was observed near the shaft, the present results exhibit a more pronounced reduction of stress with the increase of h/R, consistent with the experimental results. These stress relaxations could also be caused by linked to ongoing shear zone contraction, as discussed later in the paper, and the peak radial stress at h/R = 30 is half of that at h/R = 6, a trend which is more consistent with the experimental findings.

The cylindrical stress equilibrium conditions lead to circumferential stresses varying steeply near the pile shaft leading to $\sigma'_r < \sigma'_\theta$ in the near shaft zone as a natural consequence, set out by Jardine et al. (2013b) and confirmed by numerical simulations of Yang et al. (2020) and Fu et al. (2023). However, the major part of the stress relaxation that takes place between the pile tip and shaft is caused by the strain path reversals that take place as the soil flows past the shoulder of the pile tip (Yang et al. 2010, Guo et al. 2023) and the strain paths developed during penetration are considered in the next section. It is noteworthy that the stationary radial stresses simulated in this study remain greater than those measured experimentally. This might be due to the cyclic loading implicit in the adopted calibration chamber pile test installation process, which is not considered in the simulation.

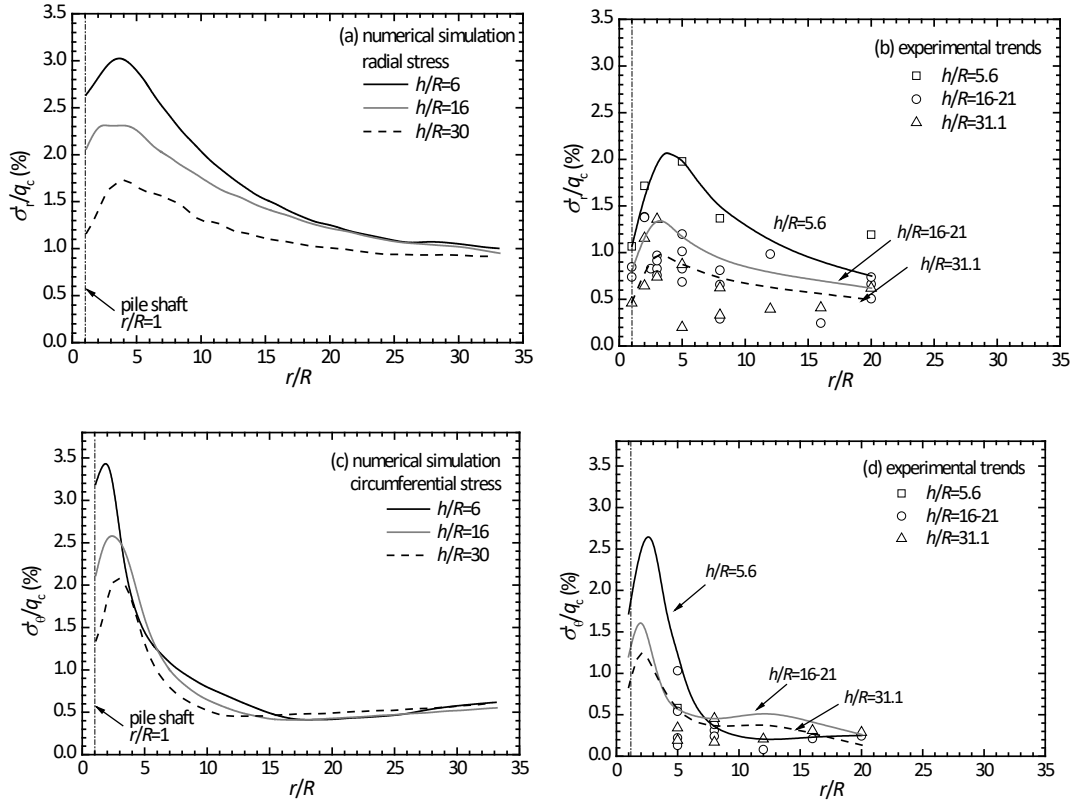

Fig. 7. Stresses above tip (h/R > 5) after end of installation: (a) numerical radial stresses (b) experimental radial stresses (c) numerical circumferential stress (d) experimental circumferential stress

The accumulative volumetric strain contours at a penetration depth L_p = 20R are illustrated in Fig. 8. Note that the volumetric strain in this study is calculated by the determinant of the deformation gradient, which is suitable for large deformation problem. A very narrow compression zone below the cone tip and extending along the shaft can be observed from Fig. 8. This localized contraction is generated by the sand crushing, as has been observed in 'post-mortem' examinations of, or PIV and DIC measurements made in, calibration chamber model pile tests (Yang et al. 2010, White and Bolton 2004, Ganju et al. 2020, Tovar-Valencia et al. 2023). A similar volumetric compression zone was predicted in ALE simulations involving grain crushing by Jin et al. (2018). The contractive behaviour of crushed sand near to the pile shaft probably is likely to contribute to the degradation of shaft radial stresses with h/R which has been observed in field and model tests (Lehane et al, 1993, Chow 1997, Jardine et al. 2013a, b). The near shaft contraction

reflects the particle rearrangement that occurs in the shear band and is linked to the migration of crushed fine particles from the pile–soil interface into the uncrushed zone in the far field. The more generally dominant dilation caused by shearing the dense sand emerges from r/R = 1 and extends to 8~10 radially with $\varepsilon_v \geq 0.5\%$ above the pile tip.

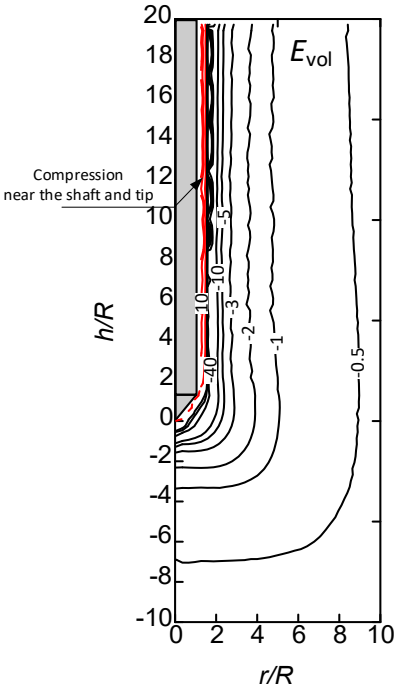

Fig. 8. Post-installation accumulative volumetric strain (values in percentage) after penetrating to L_p/R = 20

3.2 Simulation of Purdue DIC chamber test- verification of displacement and strain field

The half-pile monotonically jacked penetration tests conducted by Arshad (2014) in Purdue University are simulated using the same axisymmetric MPM model, but with the focus placed on the deformation and strain in the penetration process. The solid brass pile, with a cone tip diameter of 31.75 mm and a total length of 0.915 m, is treated as a rigid body, and is embedded to a final depth of 0.6 m (L_p), resulting in $L_p/R \approx 38$. The sand mass is considered as a deformable material simulated by the aforementioned breakage model. To minimize the boundary effects, the same dimensions as the calibration chamber are used, with a radial width (half diameter) of w = 0.84 m and a height of 1.2 m, resulting in w/R ratio of approximately 53 (Ghionna and Jamiolkowski 1991;

Salgado et al. 1998). The pile–soil interface is modelled using the modified Bardenhagen's contact method (Bardenhagen et al. 2000). The penalty friction formulation is used with a friction coefficient of 0.396 (or interface angle δ' = 21.6°), as obtained in interface shear tests by Arshad (2014) on a brass interface with the same surface roughness as the model pile.

The #2Q-ROK sand employed for the experiments is a coarse-grained, angular silica sand, mined from the Oriskany sandstone deposits at Berkeley Springs in West Virginia. Drained triaxial compression tests conducted at different confining pressures (Fu et al. 2023) show that the critical state stress ratio can be taken as M = 1.29, giving φ' = 32.1°. The breakage properties assigned to #2Q-ROK sand in the simulations are outlined in Table 2. The non-dimensional bulk and shear stiffness coefficients $\bar{K}$ and $\bar{G}$ of #2Q-ROK sand were deduced from the Poisson's ratio (taken as 0.25 after Wichtmann and Triantafyllidis. 2010) and resonant column tests conducted by the Authors, leading to a maximum Young's modulus of 65 MPa under the confining stress of 50 kPa. The critical breakage energy E_c is calculated from the yield pressure in one-dimensional compression p_{cr} = 6 MPa from Espinoza Chavez (2016). The value of γ is set as 0.85, as recommended by Tengattini et al. (2016). Other index properties in the Table 2 are from Arshad (2014).

Table 2 Model parameters of the #2Q-ROK sand.

Mechanical parameters					Index properties				
$\bar{K}$	$\bar{G}$	E_c MPa	M	γ	α_u	α_l	u'	l	θ
595	355	0.3	1.29	0.85	0.499	0.401	0.25	0.25	0.83

Fig. 9 shows the q_c profiles obtained by MPM simulation with the parameters in Table 2. The profiles stabilized at around 10 MPa when L_p > 10R. The simulated q_c is slightly steeper than the experimental curve at the shallow penetration depth but reaches a similar and relatively stable

limit of 10 MPa approximately when $L_p/R > 10$.

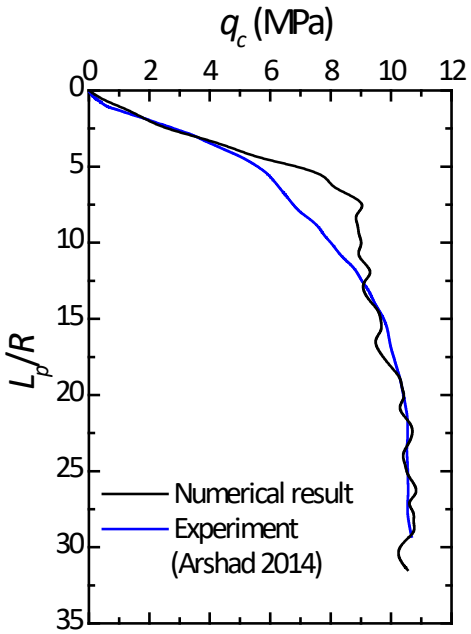

Fig. 9. Cone tip resistance profiles

The distribution of displacement vector directions is influenced by various factors, including the sand density and crushability, and pile shaft roughness. In Fig. 10, four zones are partitioned to characterize the different displacement patterns during the cone penetration, according to Arshad et al. (2014). Zone I is primarily a vertical compression region below the cone tip; zone II is a collection of crushed particle attached to the surfaces of both the cone tip and shaft, which forms a shear zone after the continuous and intense shear loading. Zone III is a transition zone, where the displacement gradually changes from vertical dominating to horizontal dominating. In zone IV, the radial displacement prevails.

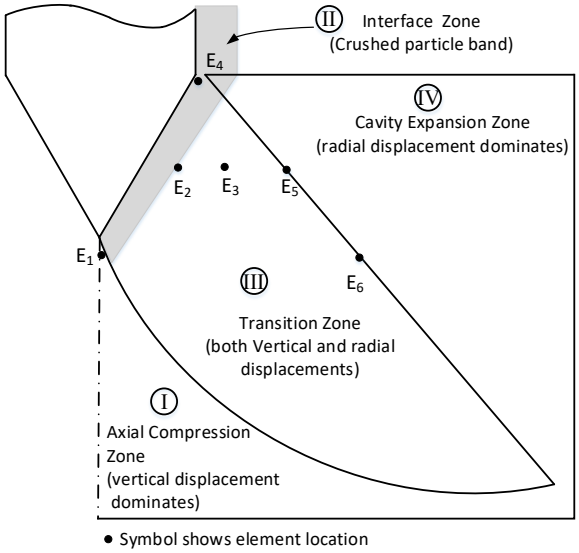

Fig. 10. Displacement zones with the proposed criterion of the partitioned zones (after Arshad et al. 2014)

Fig. 11 compares the numerical and experimental incremental soil displacements at different zones. To highlight the effect of crushing during pile penetration, the normalized displacement of soil elements (labelled E_1 to E_6 in Fig. 10) is extracted in each zone for a penetration of about 1R at the depth of 20R.

In the earlier study by Fu et al. (2023), in which no particle breakage was considered, the radial displacement increment of E_4 was significantly smaller than the vertical one and was inconsistent with the experiment. However, the displacements simulated by Martinelli et al. (2021) using a hardening soil model in MPM analyses greatly over-predicted the experimental measurements, especially in the vertical direction. These undesired outcomes were avoided in this study by employing the constitutive model that addresses particle breakage in this study. As shown in Figure 11, better good agreement was obtained between the numerical and experimental trends, confirming the good performance of the breakage model. E_1 is located at the intersection of zones I, II, and III and subjected to intensive shearing and severe particle crushing, with dominating vertical displacement. E_2 is located at the intersection of zones II and III. The incremental radial

displacement of E_2 is much larger than that of E_1, indicating that the radial displacement gradually increases along the radial direction. E_3 is located at the middle of the radial direction of region III. As the radial distance from the pile axis increases, the ratio of radial displacement to vertical displacement gradually increases, implying the radial displacement increment gradually dominates. E_4 is located near the pile shoulder in the shear band, where the radial displacement prevails. E_5 and E_6 are at the interface between zones III and IV, where radial displacement is greater than vertical displacement. The vertical displacement increments in E_4, E_5, E_6 are significantly smaller than those simulated by ALE without consideration of particle crushing in Fu et al. (2023), which indicates the deformation pattern is more consistent with the experimental measurements after considering the particle crushing.

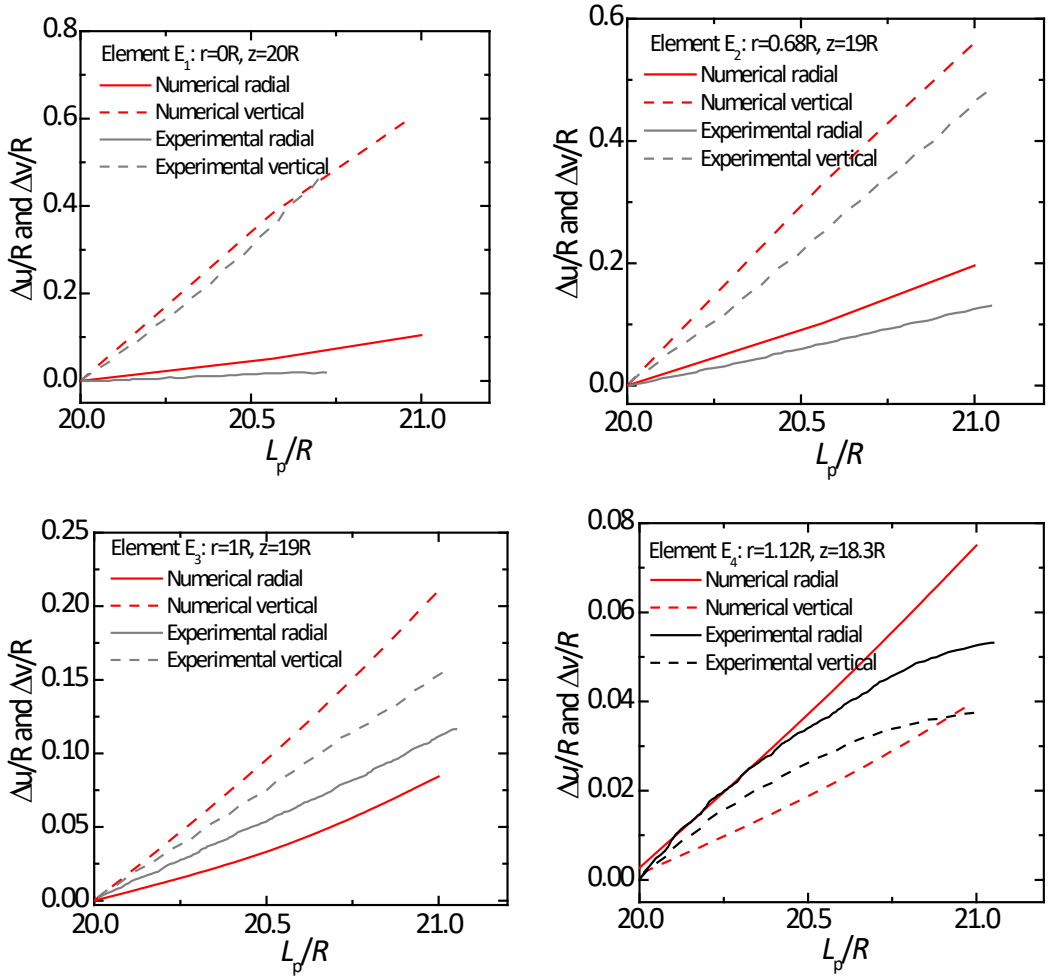

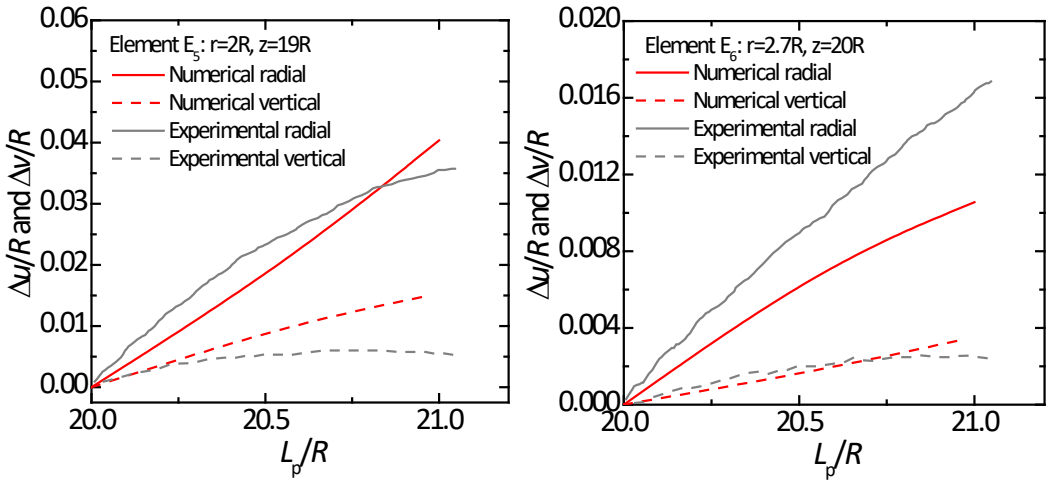

Fig. 11. Evolution of radial and vertical displacements for 1*R* penetration in different zones

Fig. 12 compares the displacement paths for a penetration depth of approximately 30*R* between the experimental results and numerical simulations, at various radial offsets from the cone penetration axis (*r*/*R* values of 0.5, 1, 1.5, 2, 3, 4, 6, and 8). The figure clearly indicates a significant concentration of movement in the near-field region around the shaft, and the trajectories rotate anti-clockwise when the radial distance of the elements increases. Specifically, the element closer to the pile shaft (elements A–D) experiences dominantly vertical motion, while that is farther away (elements E–H) moves nearly radially. The vertical displacement at element A falls closer to the measured data than the prediction by Fu et al. (2023) that did not consider particle breakage. Broadly general agreement is obtained between the numerical and experimental results.

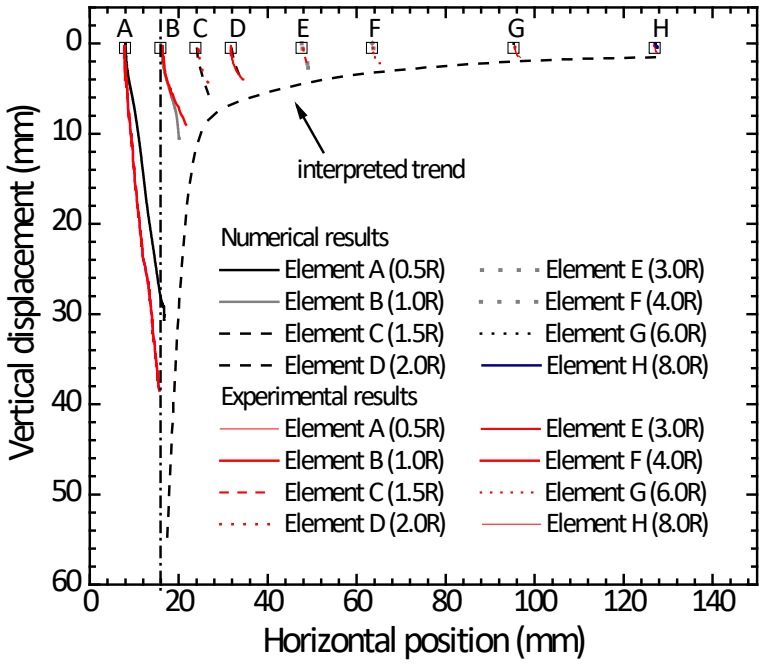

Fig. 12. Displacement paths during cone penetration from z=0R to z= 30R for different soil elements.

Fig. 13 exhibits the evolution of the normalized vertical and radial displacements of soil elements B, C, D and E against the cone penetrates from L_p = 0 to 25R (the same as experiment). These plots clearly show the four stages of simulated displacement evolution patterns, which are consistent with the experimental results (Arshad et al. 2014) and numerical simulations (Gao et al. 2022, Fu et al. 2023). Note that the vertical displacements predicted in the present simulation are clearly smaller than those found by Fu et al. (2023) without considering particle crushing. It can be observed that particle crushing leads to an inward radial displacement after stage 3, capturing the feature observed in the experiments. The reversal displacement in this study may be attributable to the compression zone comprising the crushed fine particles near the pile tip and shaft, which results in an inward movement of sand particles. Furthermore, the reverse motion of the horizontal displacement observed in the numerical simulations after the pile tip has advanced to greater depth could also provide a possible explanation for the h/R effect. Radial displacement towards the cone shaft is an indicator of radial stress relaxation (unloading in the radial direction), as

observed in calibration chamber tests (White and Bolton, 2004, Arshad et al. 2014).

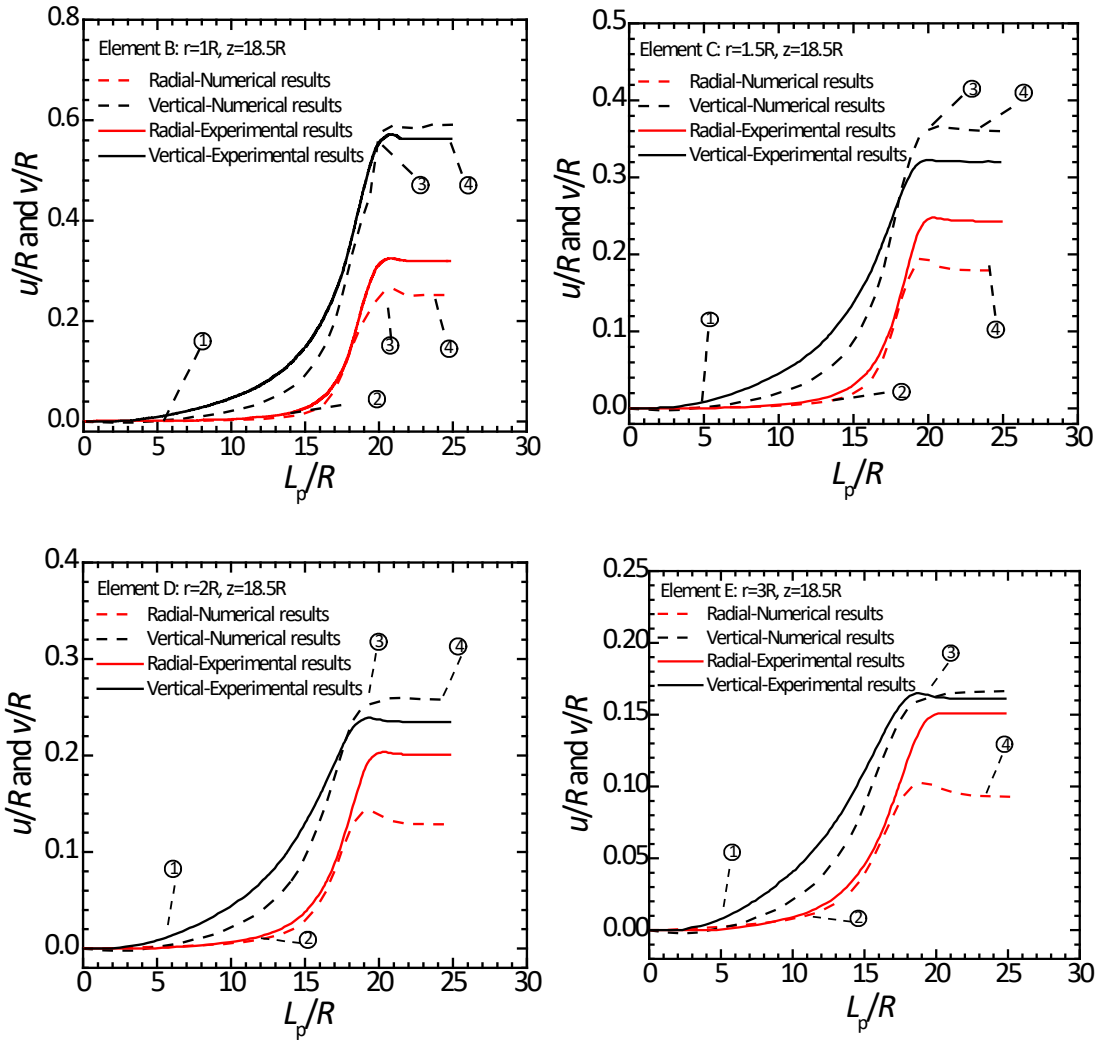

Fig. 13. Evolution of normalized radial and vertical displacements of soil elements at different locations during the cone penetration

Fig. 14 shows the strain paths of soil elements for the cone penetration from L_p = 0 to 25R in both numerical simulations and experimental tests, with E_{xx}, E_{yy} and E_{xy} for radial, vertical and shear strains respectively. It can be seen that the numerical trends are broadly consistent with the experimental counterparts. In Fig. 14, both vertical and radial strains undergo a reversal after the pile tip passing through the soil element levels, with the vertical strain changing from compression to tension, while the radial strain direction being opposite to that of the vertical strain. Although there are still considerable discrepancies between the simulated and experimental results, the

numerical analyses capture key aspects of the strain reversal phenomena that apply over the final stages of model pile penetration.

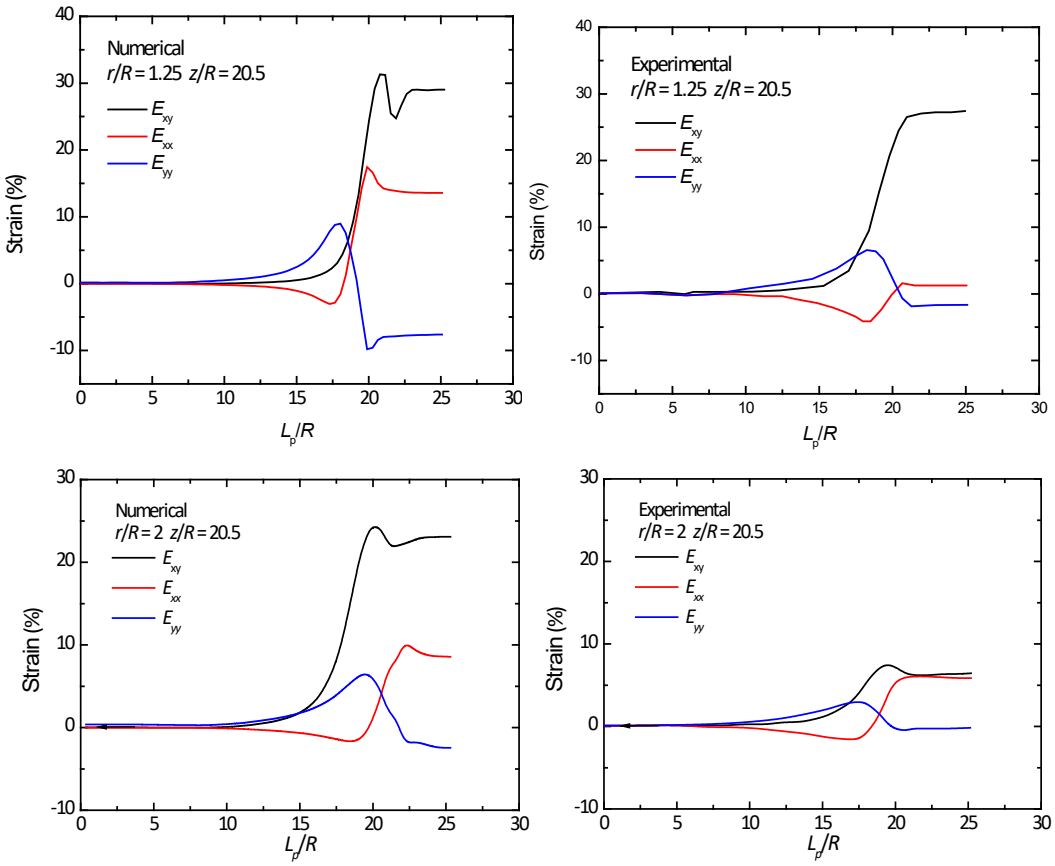

Fig. 14. Strain paths during continuous cone penetration from $L_p = 0R$ to $L_p = 25R$

Fig. 15 compares the incremental volumetric strain (E_{vol}) patterns in MPM simulation and experimental results when the tip at the depth of 20R. The incremental volumetric strain contours indicate the presence of a contractive zone (maximum contraction of 3% in numerical simulation and 2% in experiments), that is sandwiched between dilative zone and axisymmetric boundary (with a dilation of ≈ 2-4%) along the axis of cone penetration.

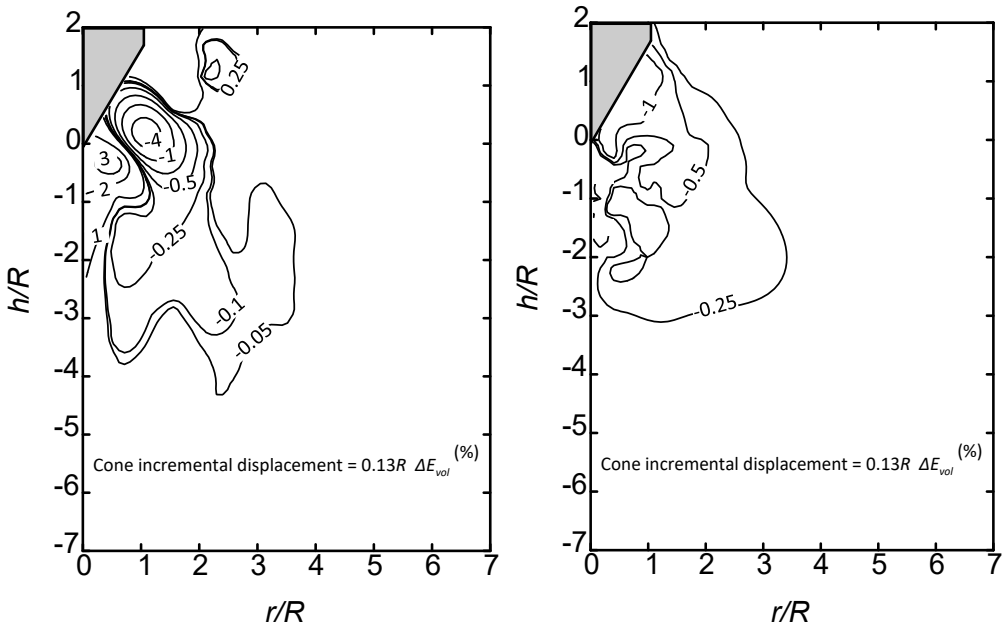

Fig. 15. Volumetric strain (E_{vol}) increments at L_p = 20R: (a) numerical results; (b) experimental results

Fig. 16 exhibits the spatial distribution of volumetric strains for both the numerical simulation and experiment for the pile penetration from L_p = 0 to 20R. The volumetric strain contour maps indicate that different dilation and compression zones observed between the experiments and simulations. A compression zone is observed immediately beneath the cone tip in the experiment, and its size is thinner than that in the numerical simulations. According to the numerical results, the sand particles are first crushed in the vicinity of the pile tip, and these crushed particles then 'coat' the shaft as the pile further penetrates. Therefore, a thin compression layer adhering to the shaft is observed, while it is absent in the experiments, possibly owing to the accuracy of DIC technique. The possible migration of crushed particles along the pile–soil interface would cause soil stress 'relaxation' in the region adjacent to the interface. Extreme shear strains are developed along the shaft, leading to volume contraction, while significant dilation occurs away from the cone tip and shaft regions, as consistently observed in both simulations and experiments.

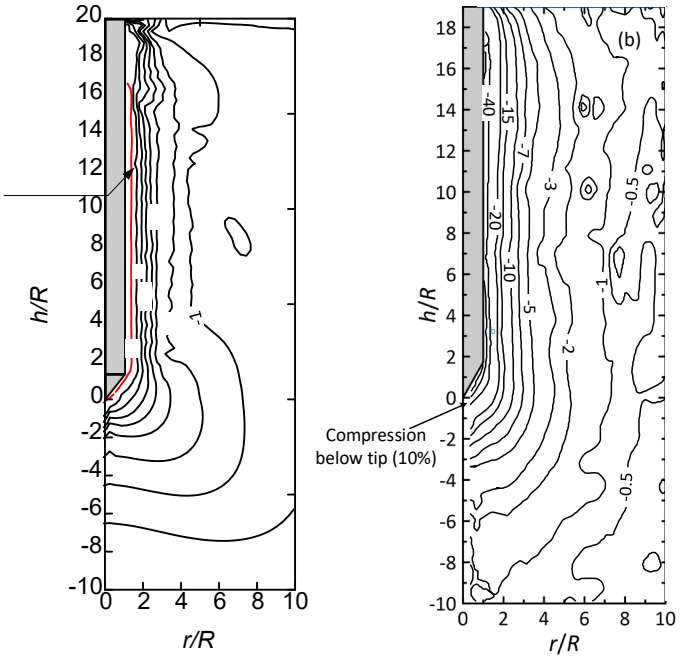

Fig. 16. Post-installation cumulative volumetric strain after penetrating to L_p/R = 20 (a) numerical result; (b) experimental result

Fig. 17 compares the evolution of volumetric strain for soil elements at z = 18.5R for pile penetration from L_p = 0 to 25R between the numerical and experimental results. The element near the cone penetration path (r = 1.25R) exhibits a strongly dilative response in both the numerical simulations and the experiments. However, the element immediately beneath the pile tip (r = 0R), displays intense contraction in the numerical simulation, where no experimental observation could be made by Arshad (2014). As discussed in Yang et al. (2010), the sand beneath the pile tip undergoes the axial compression and is squeezed out horizontally by the further penetration, resulting in a significant massive reduction in local radial stress as the pile tip passes by. However, for the elements with greater r/R, gradually suppressed dilative response is observed in both numerical simulation and experiment.

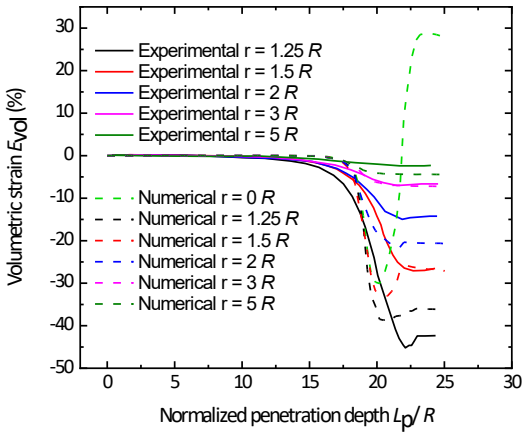

Fig. 17. Evolution of volumetric strain paths of soil elements at r/R = 0, 1.25, 1.5, 2, 3, and 5 at z = 18.5R

Fig. 18 compares the incremental volumetric strain between the numerical simulations and experiments for soil elements located at normalized radial offsets of r/R = 0, 1.25, 1.5, 2, 3 from the cone axis for an incremental penetration of 1R from L_p/R = 20 to 21. Both the numerical simulations and experiments indicate that the soil element at r = 0R contracts. As shown in the experiment, except for the element at r = 0R, all the others dilate. However, in the numerical simulation, the elements at r = 0R and 1.25R both contract, indicating that the volume compression area obtained by numerical simulation is larger than it appears in the experiments. This discrepancy could be attributed to the limitations of DIC technology. Specifically, after the particle crushing, the volume evolution of the particle cannot be accurately detected by DIC, leading to an underestimation of the size of the compression zone.

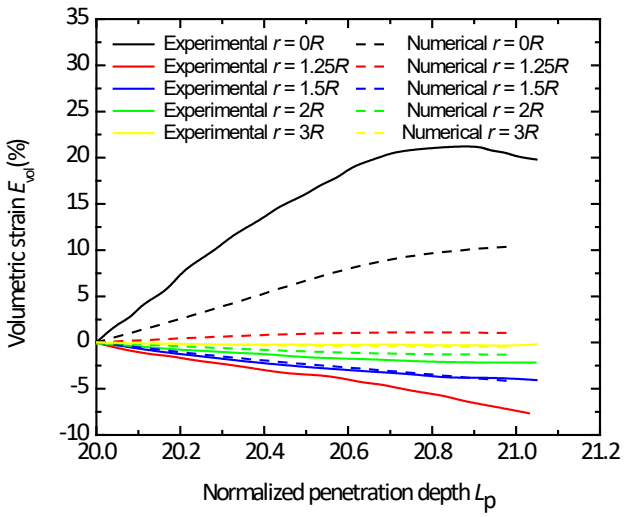

Fig. 18. Evolution of incremental volumetric strain paths of soil elements at r/R = 0, 1.25, 1.5, 2, 3 at z = 20R during an incremental penetration of 1R

It is noteworthy that the volume change near the pile shaft is very difficult to measure experimentally due to the optical feature changes (reflection) of the crushed particles, which reduces the accuracy of DIC or PIV observations. The numerical analysis provides credible information on the volumetric straining in the near-field region (r/R < 2) which could not be measured accurately.

It is meaningful to compare the pile shaft stresses obtained from the MPM analysis with the predicted results based on CPT design methods for better evaluation of the pile bearing capacity. Fig. 19 shows the normalized radial stress distribution over the pile shaft predicted by the MPM for a penetration depth of 600 mm. The design profiles from the ICP-05 (Jardine et al. 2005) and UWA-05 (Lehane et al. 2005) design methods for piles driven in sands are also presented. As remarked earlier, the numerical simulations show significantly higher stationary shaft radial stresses than the design methods over most of the shaft length (at times between 10 and 30 days after driving) and far steeper variations within the h < 2R region 'near-tip' region. The significant discrepancy may be due to the present simulation of monotonic penetration instead of cyclic

dynamic field driving. Note also that the analysis does not capture any of the ageing effects that occur in the field after driving, which are discussed by Jardine(2023).

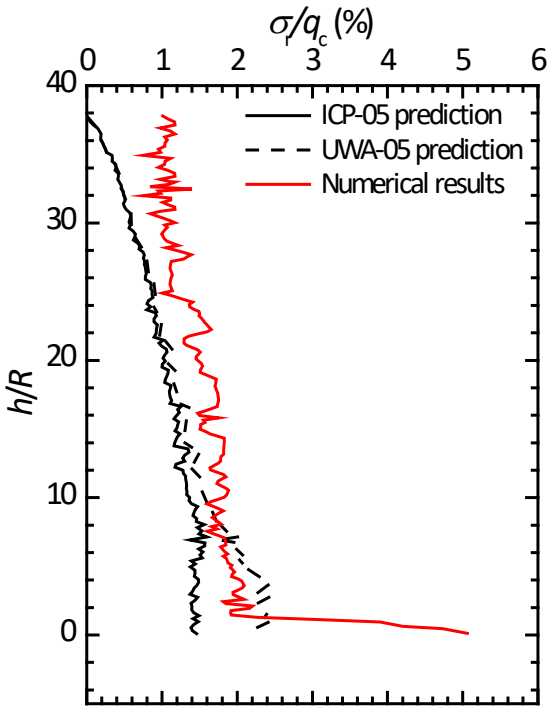

Fig. 19. Shaft radial stresses normalized by q_c at the depth of 600 mm.

4. Summary and conclusions

This paper has set out MPM simulations of pile or CPT cone penetration into silica sand. A thermodynamic based constitutive model was employed that can simulate both contractive and dilative sand response as well as grain crushing effect under high confining pressure, with model parameters calibrated against the laboratory tests on Fontainebleau NE34 and #2Q-ROK sands. The MPM analyses delivered predictions for the stress, deformation and strain fields developed during and after the penetration. Comparing the numerical results with well-documented calibration chamber test results allowed the predictions, and the impact of grain crushing, to be interpreted and discussed, leading to the following conclusions:

1. The MPM analysis employing the thermodynamic based breakage model was able to capture the most prominent features of pile penetration into the crushable sand and offer

representative quantitative predictions for measurements in the calibration chamber tests. The treatment offered more comprehensive and accurate predictions than previous ALE analyses employing Mohr–Coulomb sand models.

2. The numerically predicted displacements and strains showed good quantitative agreement with the complex patterns established experimentally in the Purdue DIC chamber test. The breakage model can reasonably capture the volume compression caused by particle breakage in the vicinity of the pile shaft that was not captured by previous studies which neglected particle breakage. Compression of the sand due to particle breakage leads to significant volume changes, which offset the influence of dilation due to grain rearrangement. The relationship between the contraction and particle breakage is highlighted in the present simulations.

3. An interface zone adjacent to the pile shaft comprising crushed soil particles was predicted that contracted in the simulations. The compression zone developed near the pile shaft is caused by irrecoverable particle breakage, which offers a possible mechanism for much of the h/R effect that occurs in the field after the major impact of the radial displacement reversal associated with the geometry of sand 'flow' around the pile tip.

4. The stress and GSD distributions predicted within the sand mass showed good qualitative agreement with measurements made in the 'Grenoble' calibration chamber tests. Both the sand grain size distribution changes and the patterns of sand stresses were predicted with reasonable accuracy.

5. However, the constitutive model employed for the sand did not capture additional effects related to the cyclic loading implicit in the Grenoble model pile experiments, nor the locally dilative mechanism induced in the shaft shear zone by the pile's surface roughness. These

unmodelled features are interpreted as being the cause of some discrepancies between the observed and measured sand stresses.

6. While this study provides valuable insights into the use of MPM for simulating geotechnical problems and opens up new opportunities for further research in this area, more sophisticated hysteretic sand constitutive models and sand-to-rough steel interface shear laws appear necessary to achieve more accurate analytical predictions.

CRedit authorship contribution statement

S. Fu: Methodology, Formal analysis, Writing–original draft. **Z.X. Yang**: Conceptualization, Methodology, Writing–review & editing, Supervision, Funding acquisition. **N. Guo**: Methodology, Writing–review & editing, Supervision. **R.J. Jardine**: Methodology, Writing–review & editing, Supervision.

Declaration of Competing Interest

The authors declare that they have no known competing financial interests or personal relationships that could have appeared to influence the work reported in this paper.

Data availability

The data generated in this study are available from the corresponding author upon reasonable request.

Acknowledgement

This research was supported by the Key R&D Program of Zhejiang Province (No. 2022C03180) and

Natural Science Foundation of China (Nos. 52020105003 and 52338008).

Notations

A	symbol linked to the pressure-dependent model
B	breakage variable
E_B, E_C	breakage energy and critical breakage energy respectively
E_{xx}, E_{yy}, E_{xy}	radial strains, vertical strains and shear strains respectively
E_{vol}	volumetric strain
H	the tip relative position
$\bar{G}$	non-dimensional shear stiffness coefficients
$\bar{K}$	non-dimensional bulk stiffness coefficients
L	controlling the evolution of limiting minimum porosity with breakage
L_p	penetration length
M	critical state stress ratio
p_{cr}, p_r	the yield pressure in the isotropic compression and reference pressure
q_c	pile tip resistance
r, R	radial distance to the pile and radius of the pile respectively
W	radial width (half diameter) of the calibration chamber
u, v	radial displacement and vertical displacement
u'	controlling the evolution of limiting maximum porosity with breakage
Y	yield surface
Z	penetration depth
α_u, α_l	minimum and maximum porosity at breakage B = 0
δ'	interface angle
ϕ_{max}, ϕ_{min}, ϕ	the maximum, minimum and current porosities respectively
Γ	material parameter, controlling its tendency to dilate
φ'	internal friction angle
Λ	plastic multiplier
Ω	coupling angle between crushing and fragment rearrangement
θ	the grading index of GSDs
σ'_r, σ'_θ	radial stresses and circumferential stresses respectively
T	relative porosity
Ψ	Helmholtz free energy
Δu, Δv	radial displacement increments and vertical displacement increments

References

Altuhafi, F., Jardine, R.J., Georgiannou, V.N., and Sim, W. (2018). “Effects of particle breakage and

stress reversal on the behaviour of sand around displacement piles." Géotechnique. 68 (6): pp. 546-555.

API (American Petroleum Institute). 2014. ANSI/API recommended practice 2GEO. 1st Ed., RP2GEO. Washington, DC: API.

Andersen, S., Andersen, L. 2010. "Modelling of landslides with the material-point method." Comput Geosci, 14(1):137–147.

Andria- Ntoanina, J., Canou, J. and Dupla, J. C. 2010. "Caractérisation mécanique du sable de Fontainebleau NE34 à l'appareil triaxial sous cisaillement monotone." Laboratoire Navier - Géotechnique (CERMES, ENPC/LCPC).

Arshad, M.I. 2014. "Experimental study of the displacements caused by cone penetration in sand." Ph.D. thesis, Purdue University.

Arshad, M.I., Tehrani, F.S., Prezzi, M., and Salgado, R. 2014. "Experimental study of cone penetration in silica sand using digital image correlation." Géotechnique 64(7), 551-569.

Bardenhagen, S.G., Brackbill, J.U., Sulsky, D., 2000. "The material-point method for granular materials." Comput. Meth. Appl. Mech. Eng. 187 (3–4), 529–541.

Bardenhagen, S.G., Guilkey, J.E., Roessig, K.M., Brackbill, J.U., Witzel, W.M., and Foster, J.C. 2001. "An improved contact algorithm for the material point method and application to stress propagation in granular materials." Comput. Model Eng. Sci. 2(4), 509–522

Bardenhagen, S.G., Kober, E.M., 2004. "The generalized interpolation material point method." CMES-Comput. Model. Eng. Sci. 5 (6), 477–495.

Cathie D., Jardine, R. J, Silvano, R., Kontoe, S. and Schroeder. F 2022. "Pile setup in sand – the "PAGE" joint industry project." Proc. 11th International Conference on Stress Wave Theory and

Design and Testing Methods for Deep Foundations. Rotterdam. Sept 2022. Pub. KVI, The Hague, The Netherlands.

Chong, F. 1988. “Density changes of sand on cone penetration resistance.” Proc. 1st Symp. Penetration Testing, ISOPT-1, 2, 707–714. Rotterdam: Balkema.

Chow, F.C. 1997. "Investigations into displacement pile behaviour for offshore foundations." Ph.D. thesis, Imperial College, London.

Ciantia, M., O’Sullivan, C., and Jardine, R.J. 2019. “Pile penetration in crushable soils: Insights from micromechanical modelling.” 17th European Conference on soil Mechanics and Geotechnical Engineering (ECSMGE 2019). 1-20.

Dano, C., Hicher, P. Y., Tailliez, S. 2004. ”Engineering Properties of Grouted Sands.” J. Geotech. Geoenviron. Eng. 130(3): 328-338.

de Vaucorbeil, A., Nguyen, V. P., Sinaie, S., Wu, J. Y. (2020). "Material point method after 25 years: Theory, implementation, and applications." Advances in applied mechanics 53: 185-398.

Dong, Y. 2020. “Reseeding of particles in the material point method for soil–structure interactions.” Comput. Geotech. 127, 103716.

Einav, I. 2007a. “Breakage mechanics. Part I: theory. ” J. Mech. Phys. Solids 55, No. 6, 1274–1297.

Einav, I. 2007b. “Breakage mechanics. Part II: modelling granular materials.” J. Mech. Phys. Solids 55, No. 6, 1298–1320.

Fu, S., Yang, Z. X., Jardine, R. J. & Guo, N. (2023). “Large deformation finite element simulation of deformation and strain fields resulting from closed-end displacement pile installation in sand.” J. Geotech. Geoenviron. Eng. 149(6), 04023038.

Ganju, E., Han, F., Prezzi, M., Salgado, R., Pereira, J. S. 2020. “Quantification of displacement and

particle crushing around a penetrometer tip." Geosci. Front., 11(2), 389-399.

Gao, L., Guo, N., Yang, Z.X., and Jardine, R.J. 2022. "MPM modeling of pile installation in sand: Contact improvement and quantitative analysis." Comput. Geotech. 151, 104943.

Gavin, K.G., and Lehane, B.M. 2003. "The shaft capacity of pipe piles in sand." Can. Geotech. J. 40(1), 36-45.

Ghionna, V.N., and Jamiolkowski, M. 1991. "A critical appraisal of calibration chamber testing of sands." In Proceedings of the 1st International Conference on Calibration Chamber Testing, Clarkson Univ. Potsdam, USA, 13-37.

Guo, N., Liu, H.F., Li, B.J., and Yang, Z.X., 2023. "DEM study of the stress fields around the closed-ended displacement pile driven in sand." Can. Geotech. J., in press.

Hammerquist, C.C., Nairn, J.A., 2018. "Modeling nanoindentation using the material point method." J. Mater. Res. 33, 1369–1381.

Ho, Y.K., Jardine, R.J and Anh-Minh, N. (2011). Large displacement interface shear between steel and granular media. Géotechnique, Vol 61, No. 3, pp. 221-234.

Jardine, R.J., Chow, F.C., Overy, R., and Standing, J.R. 2005. ICP design methods for driven piles in sands and clays. London: Thomas Telford.

Jardine, R. J., Standing, J. R. & Chow, F. C. (2006). Some observations of the effects of time on the capacity of piles driven in sand. Géotechnique 55 (4), pp. 27–244.

Jardine, R.J., Zhu, B.T., Foray, P., and Yang, Z.X. 2013a. "Measurement of stresses around closed-ended displacement piles in sand." Géotechnique 63(1), 1-17.

Jardine, R.J., Zhu, B.T., Foray, P., and Yang, Z.X. 2013b. "Interpretation of stress measurements made around closed-ended displacement piles in sand." Géotechnique 63(8), 613-627.

Jardine, R.J., and Yang, Z.X. 2018. “Joint research into the behaviour of driven piles.” In Proceedings of China-Europe Conference on Geotechnical Engineering, SSGG, edited by W. Wu and H.-S. Yu, 961-972.

Jardine, R.J. 2020. “Geotechnics, energy and climate change: the 56th Rankine Lecture.” Géotechnique 70(1): 3-59.

Jardine, R.J. (2023). “Time-dependent vertical bearing behaviour of shallow foundations and driven piles.” 6th ISSMGE McClelland Lecture. Proc. 9th Int. Conf. on Offshore Site Investigations and Geotechnics, SUT London.

Jin, Y. F., Yin, Z. Y., Wu, Z. X., Daouadji, A. 2018. “Numerical modeling of pile penetration in silica sands considering the effect of grain breakage.” Finite Elem. Anal. Des. 144, 15-29.

Kishida, H., and Uesugi, M. 1987. “Tests of the interface between sand and steel in the simple shear apparatus.” Géotechnique 37(1), 45–52.

Klotz, E. U., Coop, M. R. 2001. “An investigation of the effect of soil state on the capacity of driven piles in sands.” Géotechnique 51(6), 733–751.

Lehane, B.M., Jardine, R.J., Bond, A.J., and Frank, R. 1993. "Mechanisms of shaft friction in sand from instrumented pile tests." J. Geotech. Eng. 119(1), 19-35.

Lehane, B.M., Lim, J. K., Carotenuto, P., Nadim, F., Lacasse, S., Jardine, R.J., and van Dijk, B.F.J. 2017. "Characteristics of unified databases for driven piles." In Proc., 8th International Conference, Offshore Site Investigation and Geotechnics: Smart solutions for future offshore developments. 162-191.

Lehane, B.M., Liu, L., Bittar, E., Nadim, F., Lacasse, S., Jardine, R.J., Carotenuto, P., Rattley, M., Jeanjean, P., Gavin, K., Gilbert, R., Haavik, J.B., Morgan, N. (2020). “A new ‘unified’ CPT-based

axial pile capacity design method for driven piles in sand." Proc. International Symposium on Frontiers in Offshore Geotechnics (ISFOG), Austin, Texas, pp. 462-477.

Liu, W. 2010. “Axisymmetric centrifuge modelling of deep penetration in sand.” Ph.D. thesis, University of Nottingham.

Lorenzo, R., da Cunha, R.P., Neto, M.P.C., and Nairn, J.A. 2018. "Numerical simulation of installation of jacked piles in sand using material point method." Can. Geotech. J. 55(1), 131-146.

Luong, M., Touati, A., 1983. “ Sols grenus sous fortes contraintes. ” Rev. Fr. Géotech. (24), 51–63.

Ma, J., Wang, D., Randolph, M.F., 2014. “A new contact algorithm in the material point method for geotechnical simulations.” Int. J. Numer. Anal. Meth. Geomech. 38 (11), 1197–1210.

Martinelli, M., Galavi, V. 2021 “Investigation of the Material Point Method in the simulation of Cone Penetration Tests in dry sand.” Comput. Geotech. 130, 103923,

Mo, P.Q., Marshall, A.M., Yu, H.S. 2015 “Centrifuge modelling of cone penetration tests in layered soils.” Géotechnique 65(6), 468-481.

Ngan-Tillard, D.J.M., Cheng. X.H., van Nes, J., Zitha, P.L.J. 2005. “Application of x-ray computed tomography to cone penetration tests in sands.” In GSP 138 Site Characterization and Modeling, 1-12.

Otani, J., Mukunoki, T., Sugawara, K. 2005. “Evaluation of particle crushing in soils using X-ray CT data.” Soil Found. 45(1), 99-108.

Phuong, N.T.V., van Tol, A.F., Elkadi, A.S.K., and Rohe, A. 2016. "Numerical investigation of pile installation effects in sand using material point method." Comput. Geotech. 73, 58-71.

Robinsky, E.I., and Morrison, C.F. 1964. "Sand displacement and compaction around model friction piles." Can. Geotech. J. 1(2), 81-93.

Sadeghirad, A., Brannon, R.M., Burghardt, J., 2011. “A convected particle domain interpolation technique to extend applicability of the material point method for problems involving massive deformations.” Int. J. Numer. Meth. Eng. 86, 1435–1456.

Salgado, R., Mitchell, J.K., and Jamiolkowski, M. 1998. "Calibration chamber size effects on penetration resistance in sand." J. Geotech. Geoenviron. Eng. 124(9), 878-888.

Salgado, R., Bisht, V., Prezzi, M. 2022. “Material Point Method simulations of cone penetration and CPT interpretation.” Cone Penetration Testing 2022. CRC Press, 16-27.

Soga, K., Alonso, E., Yerro, A., Kumar, K., Bandara, S. 2016. “Trends in large-deformation analysis of landslide mass movements with particular emphasis on the material point method.” Géotechnique, 66(3), 248-273.

Steffen, M., Kirby, R.M., Berzins, M., 2008. “Analysis and reduction of quadrature errors in the material point method (MPM).” Int. J. Numer. Meth. Eng. 76 (6), 922–948.

Tehrani, F.S., Arshad, M.I., Prezzi, M., and Salgado, R. 2018. "Physical modeling of cone penetration in layered sand." J. Geotech. Geoenviron. Eng. 144(1), 04017101.

Tengattini, A., Das, A., Einav, I. 2016. A constitutive modelling framework predicting critical state in sand undergoing crushing and dilation. Géotechnique, 66(9), 695-710.

Tovar-Valencia, R.D., Galvis-Castro, A., Salgado, R., and Prezzi, M. 2018. "Effect of surface roughness on the shaft resistance of displacement model piles in sand." J. Geotech. Geoenviron. Eng. 144(3), 04017120.

Tovar-Valencia, R.D., Galvis-Castro, A., Salgado, R., Prezzi, M, Fridman, D. 2023. “Experimental measurement of particle crushing around model piles jacked in a calibration chamber.” Acta Geotech. 18, 1331–1351

Tsuha, C.H.C., Foray, P.Y., Jardine, R.J., Yang, Z.X., Silva, M., and Rimoy, S. 2012. "Behaviour of displacement piles in sand under cyclic axial loading." Soil Found. 52(3), 393-410.

Wang, J., and Zhao, B. 2014. "Discrete-continuum analysis of monotonic pile penetration in crushable sands." Can. Geotech. J. 51(10), 1095-1110.

White, D.J. 2002. “An inverstigation into the behavior of pressed-in piles.” PhD thesis, Cambridge University.

White, D.J., and Bolton, M.D. 2004. ”Displacement and strain paths during plane-strain model pile installation in sand.” Géotechnique 54(6), 375-397.

Espinoza Chavez, W.F. 2016. "Laboratory characterization of #2Q-ROK sand". Master thesis, Purdue University.

Wichtmann, T., Triantafyllidis, T. 2010. “On the influence of the grain size distribution curve on P-wave velocity, constrained elastic modulus Mmax and Poisson's ratio of quartz sands.” Soil Dyn. Earthq. Eng. 30(8), 757-766.

Yang, Z.X., Jardine, R.J., Zhu, B.T., Foray, P., and Tsuha, C.H.C. 2010. "Sand grain crushing and interface shearing during displacement pile installation in sand." Géotechnique 60(6), 469-482.

Yang, Z.X., Guo, W.B., Jardine, R.J., and Chow, F. 2017. "Design method reliability assessment from an extended database of axial load tests on piles driven in sand." Can. Geotech. J. 54(1), 59-74.

Yang, Z.X., Gao, Y.Y., Jardine, R.J., Guo, W.B., Wang, D. 2020. “Large deformation finite element simulation of displacement pile installation experiments in sand.” J. Geotech. Geoenviron. Eng. 146(6), 04020044

Yasufuku, N. & Hyde, A. F. L. 1995. ”Pile end-bearing capacity in crushable sands.” Géotechnique 45(4), 663–676.

Yost Kaleigh M., Mario Martinelli, Alba Yerro, Russell A. Green, Dirk A. de Lange. 2023. “Addressing complexities in MPM modeling of calibration chamber cone penetrometer tests in homogenous and highly interlayered soils.” Comput. Geotech. 158, 105378.

Zhang, C., 2012. Breakage Mechanics in Large Granular Flow Problems. The University of Sydney Ph.D. Thesis.

Zhang, C., Nguyen, G.D., and Einav, I. 2013. "The end-bearing capacity of piles penetrating into crushable soils." Géotechnique 63(5), 341-354.

Zhang, C., Yang, Z.X., Nguyen, G.D., Jardine, R.J., and Einav, I. 2014. "Theoretical breakage mechanics and experimental assessment of stresses surrounding piles penetrating into dense silica sand." Géotechnique Lett. 4, 11-16.

Zhang, D.Z., Ma, X., Giguere, P.T., 2011. Material point method enhanced by modified gradient of shape function. J. Comput. Phys. 230 (16), 6379–6398.